A STUDY OF POLOIDAL ASYMMETRIES IN TOKAMAKS

A THESIS

Presented to

The Academic Faculty

by

Danika Rae Jackson
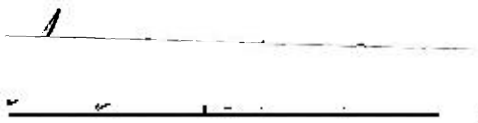
In Partial Fulfillment

of the Requirements for the Degree

Master of Science in Nuclear Engineering

Georgia Institute of Technology

September 1992

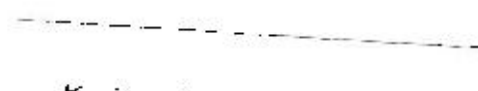# A STUDY OF POLOIDAL ASYMMETRIES IN TOKAMAKS

APPROVED:

Weston M. Stacey, Chairman

John Mandrekas

Alan V. Larson

Date Approved by Chairperson 8-18-92

ii

TABLE OF CONTENTS

LIST OF TABLES

LIST OF FIGURES

vi

LIST OF SYMBOLS

a . . . . Minor radius

B_θ . . . . . Poloidal magnetic field

B_ϕ, B_t . . Toroidal magnetic field

E . . . . Electric field

E_b . . . . . . Neutral beam energy

e . . . . Charge

f . . . . Viscosity

G . . . . . . Gradient scale factor

h_{nv}, h_{nTv} Spatial integrals

I_p . . . . . . Plasma current

j,k . . . . . . Main ion species and impurity ion species

$\mathbf{M}_j$ . . . . . . Rate of momentum input

m . . . . . . Ion mass

m_b . . . . . Mass of neutral beam ion

m_D . . . . . Deuterium mass

$\bar{m}$ . . . . . . Effective mass

n_b . . . . . . Doublet III edge density

$\bar{n}_e$ . . . . . . Line-average electron density

n_{e0} . . . . . . Central electron density

$\tilde{n}_j^c, \tilde{n}_k^c$. In-out density asymmetries

$\tilde{n}_j^s, \tilde{n}_k^s$. Up-down density asymmetries

P_b .... Neutral beam power

p ..... Pressure

Q .... Peaking factor

q ..... Safety factor

R .... Major radius

$\mathbf{R}_j$ .... Collisional friction

R_{tan} .. Tangency radius

T_e .... Electron temperature

T_i .... Ion temperature

T_{i0} ... Central ion temperature

T_{OH} .. Temperature due to ohmic heating

$\hat{v}_{jr}, \hat{v}_{kr}$ Radial velocity

$\hat{v}_{j\theta}, \hat{v}_{k\theta}$ Theoretical poloidal velocity

v_{th} ... Thermal velocity

v_ϕ^{ex} ... Experimental toroidal velocity

Z ..... Impurity charge

Z_{eff} .. Effective charge

α_n .... Density profile factor

α_T ... Temperature profile factor

α_v .... Velocity profile factor

β ..... Ratio of B_θ to B_ϕ

Γ_ϕ .... Torque input from NBI

ϵ ..... Inverse aspect ratio

$\tilde{\Theta}$ ..... Amplitude of poloidal variations in asymmetries

Λ ..... Coulomb logarithm

$\bar{\nu}_{jj}^*, \bar{\nu}_{kk}^*$ Dimensionless ion self-collision frequencies

$\bar{\nu}_{kj}^*, \bar{\nu}_{jk}^*$ Dimensionless interspecies collision frequencies

$\overset{\leftrightarrow}{\pi}_j$ ....   Viscosity tensor

τ_ϕ^{ex} ...   Experimental momentum confinement time

τ_ϕ^{th} ...   Theoretical momentum confinement time

$\tilde{\Phi}^c, \tilde{\Phi}^s$ Potential asymmetries

$\hat{\Phi}$ .....   Electrostatic potential

$\Omega_{\phi 0}^{ex}$ ...   Experimental central toroidal angular frequency

SUMMARY

A recently developed neoclassical theory has been used to model the poloidal rotation and density asymmetries in ASDEX, DIII, ISX-B, JET, and TFTR. Using measured plasma parameters and a first-principles model, the poloidal rotation velocity, the in-out density asymmetries, and the up-down density asymmetries were predicted for the hydrogenic and dominant impurity species in these plasmas. Adequate experimental data does not exist to allow a direct confirmation of the predictions. Thus the validity of the theory was confirmed indirectly by using the predicted asymmetries to calculate theoretical momentum confinement times which were then compared with the experimental momentum confinement times.

The experimental momentum confinement times ranged from 17 ms in ISX-B to 204 ms in JET H-mode plasmas. The theoretical momentum confinement times reasonably predicted the experimental momentum confinement times for each machine. Since the theoretical momentum confinement times depend directly on the poloidal velocities and density asymmetries, it can be inferred that the theory predicts the poloidal velocity and density asymmetries of the two ion species reasonably well.

Numerical analysis of the theory showed that the main ion and impurity ion poloidal velocities $\hat{v}_\theta$ were in the direction opposite the poloidal magnetic field and depended on the plasma viscosity and the inertial effects of the toroidal rotation. For more collisional impurities, the poloidal velocity was also affected by friction. The up-down density asymmetries for both ion species were affected mainly by a

combination of the viscosity and the up-down potential asymmetries, while the in-out density asymmetries depended on the toroidal velocity for both ion species.

In general, the in-out density asymmetries increased with increasing toroidal velocity for both ion species. On the other hand, the poloidal velocities and the up-down density asymmetries showed no clear dependences on any one of the dominant driving forces, indicating that some combination of forces was more important than any single force.

CHAPTER I

INTRODUCTION

Since the introduction of neutral beam injection (NBI) heating in tokamak plasmas, new theories regarding particle, energy, and momentum transport have been developed to explain the observed degradation of plasma confinement properties. Early transport theories were applicable to ohmically heated plasmas which exhibited particle velocities much smaller than the ion thermal velocity, and therefore were not capable of predicting confinement of NBI heated plasmas having $v_\phi \sim v_{th}$.

Poloidal rotation and density asymmetries have become a topic of increasing interest since they appear to affect the confinement properties of tokamak plasmas. For example, changes in poloidal rotation have been observed[1-3] in the L to H transition, and density asymmetries have been observed[4-8] in many ELM-free discharges.

Recently, a neoclassical theory[9] was developed to predict poloidal rotation and poloidal density asymmetries. The theory, derived from the fluid particle and momentum balance equations, consists of three nonlinear equations per ion species for a plasma which can be represented by one main ion species and one impurity ion species. For any given tokamak, the equations consist of several known parameters and six unknowns. The six unknowns are the poloidal velocities, the in-out density asymmetries, and the up-down density asymmetries for each ion species. The equations can be solved using a nonlinear equation solver.

1

The purposes of this thesis were to calculate the predicted density asymmetries and poloidal velocities in the tokamak experiments ASDEX, DIII, ISX-B, JET, PLT, and TFTR and to indirectly confirm these predictions by comparison with experiment. This was accomplished by first calculating the theoretical poloidal velocity and density asymmetries from the set of six nonlinear equations. Next a poloidal asymmetry factor which depends on the asymmetries was calculated. Then the theoretical momentum confinement times, which depend on the poloidal asymmetry factors and thus on the density asymmetries, were calculated. Finally the theoretical momentum confinement times were compared with experimental momentum confinement times. Since the density asymmetries and poloidal rotation velocities have not been measured in the core of any of these plasmas, this indirect comparison was the only method of determining the validity of the predicted asymmetries.

The organization of this thesis is as follows: in Chapter II, the poloidal rotation and density asymmetry theory and the computational model are presented. A discussion of the experimental plasma parameters, theoretical momentum confinement results, and asymmetry results follows in Chapter III. The theoretical results are then compared with the predictions of earlier theories in Chapter IV. Finally, the closing chapter includes conclusions and recommendations for future work.

CHAPTER II

THEORY OF POLOIDAL ROTATION AND

DENSITY ASYMMETRIES

2.1 Theory

A neoclassical theory was derived[9] to predict poloidal rotation velocities and poloidal density asymmetries in tokamak plasmas. The theory models NBI heated plasmas for which $v_\phi \sim v_{th}$ and $E/B_\theta \sim O(1)$. Kinetic theory effects were accounted for by including viscosity and friction terms[10] in the derivation of the theory.

In deriving the new theory, the fluid particle equation

$$\nabla \cdot (n_j \mathbf{v}_j) = 0 \qquad (2.1)$$

and the momentum balance equation

$$n_j m_j (\mathbf{v}_j \cdot \nabla) v_j + \nabla p_j + \nabla \cdot \overleftrightarrow{\pi}_j + e_j n_j \nabla \Phi - n_j e_j \mathbf{v}_j \times \mathbf{B} = \mathbf{R}_j + \mathbf{M}_j \qquad (2.2)$$

were solved self-consistently in the large-aspect-ratio approximation to determine the poloidal velocity $\hat{v}_\theta$ and density asymmetries $\tilde{n}^c$ and $\tilde{n}^s$ in tokamak plasmas.

The solution for the (normalized) poloidal velocity $\hat{v}_{j\theta}$, with j representing either the main ion species or the impurity ion species, may be expressed in the form

$$\hat{v}_{j\theta} = \frac{driving}{damping} = \frac{driving}{viscosity + friction - inertia}. \qquad (2.3)$$

3

In the above equation, *driving* (the driving force) is given by

$$\hat{M}_{j\theta} + \hat{v}_{jr} + \bar{\nu}_{jk}^* \sqrt{\frac{m_j}{m_k}} \hat{v}_{k\theta} - q^2 \hat{v}_{j\phi}^{ex2} \left\{ \frac{\tilde{\Phi}^s}{\epsilon} + \frac{f_j}{2\hat{v}_{j\phi}^{ex}} \left[\frac{\tilde{\Phi}^s}{\epsilon} \frac{\tilde{n}_j^s}{\epsilon} + \frac{\tilde{\Phi}^c}{\epsilon} \left(5 + \frac{\tilde{n}_j^c}{\epsilon} \right) \right] \right\} \qquad (2.4)$$

and the three *damping* terms are given by

$$viscosity = q^2 f_j \left\{ 1 + \frac{5}{6} \frac{\tilde{n}_j^c}{\epsilon} + \frac{2}{3} \frac{\tilde{n}_j^s}{\epsilon} + \frac{1}{3} \left[\left(\frac{\tilde{n}_j^s}{\epsilon} \right)^2 + \left(\frac{\tilde{n}_j^c}{\epsilon} \right)^2 \right] \right\}$$

$$+ \frac{q^2 f_j}{2} \left\{ \frac{\tilde{\Phi}^s}{\epsilon} \frac{\tilde{n}_j^s}{\epsilon} + \frac{\tilde{\Phi}^c}{\epsilon} \left(5 + \frac{\tilde{n}_j^c}{\epsilon} \right) \right\} \qquad (2.5)$$

$$friction = \bar{\nu}_{jk}^* \qquad (2.6)$$

$$inertia = q^2 \hat{v}_{j\phi}^{ex} \left(\frac{\tilde{n}_j^s}{\epsilon} + \frac{\tilde{\Phi}^s}{\epsilon} \right). \qquad (2.7)$$

By taking the $\sin\theta$ and $\cos\theta$ projections of the parallel component of Eq. (2.2), two equations (for each ion species) coupling $\tilde{n}_j^s$ and $\tilde{n}_j^c$ were obtained:

$$\left(\left(\frac{2}{3} f_j - \beta^2 \bar{\nu}_{jk}^* \right) \hat{v}_{j\theta} \right) \frac{\tilde{n}_j^s}{\epsilon} - \frac{1}{2} \frac{\tilde{n}_j^c}{\epsilon} = - \left(\hat{v}_{j\phi}^{ex} \right)^2 + \frac{1}{2} \hat{\Phi}_j \frac{\tilde{\Phi}^c}{\epsilon} - \beta^2 \bar{\nu}_{jk}^* \hat{v}_{j\theta} \frac{\tilde{n}_k^s}{\epsilon} \qquad (2.8)$$

$$\left(\left(\frac{2}{3} f_j - \beta^2 \bar{\nu}_{jk}^* \right) \hat{v}_{j\theta} \right) \frac{\tilde{n}_j^c}{\epsilon} + \frac{1}{2} \frac{\tilde{n}_j^s}{\epsilon} = -f_j \hat{v}_{j\theta} - \frac{1}{2} \hat{\Phi}_j \frac{\tilde{\Phi}^s}{\epsilon}$$

$$+ \beta^2 \bar{\nu}_{jk}^* \left(\hat{v}_{j\theta} - \sqrt{\frac{m_j}{m_k}} \hat{v}_{k\theta} \right) - \beta^2 \bar{\nu}_{jk}^* \hat{v}_{j\theta} \frac{\tilde{n}_k^c}{\epsilon} - \beta^2 \hat{v}_{jr} \qquad (2.9)$$

Equations (2.3-2.9), with j representing the impurity ion and k representing the main ion, constitute six equations with six unknowns: the poloidal velocities $(\hat{v}_{j\theta}, \hat{v}_{k\theta})$, the up-down density asymmetries $(\tilde{n}_j^s, \tilde{n}_k^s)$, and the in-out density asymmetries $(\tilde{n}_j^c, \tilde{n}_k^c)$. The six unknowns have been expanded in the form

$$x(r, \theta) = \bar{x}(r)[1 + \tilde{x}^s \sin\theta + \tilde{x}^c \cos\theta]. \qquad (2.10)$$

Some important dimensionless quantities which enter the equations are defined as follows:

$$\epsilon \equiv \frac{a}{R}$$

4

$$f_j = \frac{\bar{\nu}_{jj}^*}{\left(\epsilon^{1.5} + \bar{\nu}_{jj}^*\right)\left(1 + \bar{\nu}_{jj}^*\right)}.$$

$$\hat{v}_{j\theta} \equiv \frac{\bar{v}_{j\theta}}{\beta v_{thj}}.$$

$$\hat{v}_{j\phi}^{ex} \equiv \frac{\bar{v}_{j\phi}^{ex}}{v_{thj}}$$

$$\hat{v}_{jr} \equiv \frac{\bar{v}_{jr}}{\beta \delta_j v_{thj}}.$$

$$\hat{M}_{j\theta} \equiv \frac{\hat{M}_{j\theta}}{\bar{n}_j m_j w_j v_{thj} \beta}$$

$$\hat{\Phi}_j \equiv \frac{e_j}{\frac{1}{2} m_j v_{thj}^2} \bar{\Phi}. \tag{2.11}$$

where v_{thj} is the thermal speed, $\hat{v}_{j\theta}$, $\hat{v}_{j\phi}^{ex}$, and $\hat{v}_{jr}$ are the poloidal, experimental toroidal, and radial velocities of ion species j, respectively, $\hat{M}_{j\theta}$ is the poloidal momentum input, and $\hat{\Phi}_j$ is the electrostatic potential.

The poloidal velocity and density asymmetries, which are the main focus of this thesis, were used to determine theoretical momentum confinement times based on the neoclassical (gyroviscous) momentum transport theory and defined as[11]

$$\tau_\phi^{th} \equiv \frac{2R^2 eB}{(\tilde{\Theta} G/Z)_{eff}} \frac{h_{nTv}}{h_{nv}} \frac{\bar{m}}{m_D}. \tag{2.12}$$

In Eq. (2.12),

$$\tilde{\Theta} \equiv (4 + \frac{\tilde{n}_j^c}{\epsilon})[-\hat{v}_{j\theta}(\hat{v}_{j\phi}^{ex})^{-1}(\frac{\tilde{\Phi}^s}{\epsilon} + \frac{\tilde{n}_j^s}{\epsilon}) + \frac{\tilde{\Phi}^s}{\epsilon}] + \frac{\tilde{n}_j^s}{\epsilon}[\hat{v}_{j\theta}(\hat{v}_{j\phi}^{ex})^{-1}(2 + \frac{\tilde{\Phi}^c}{\epsilon} + \frac{\tilde{n}_j^c}{\epsilon}) - \frac{\tilde{\Phi}^c}{\epsilon}] \tag{2.13}$$

$$G \equiv \frac{2(r/a)^2(\alpha_n + \alpha_v + \alpha_T)}{1 - (r/a)^2} \tag{2.14}$$

where density, temperature, and velocity profiles are represented as parabolic to some power, $[1 - (r/a)^2]^{\alpha_x}$. The experimental momentum confinement time is defined[11] as

$$\tau_\phi^{ex} = \frac{2\pi R \int_0^{\bar{a}} \langle Rnmv_\phi \rangle r \, dr}{\Gamma_\phi} = \frac{2\pi^2 a^2 R^2 n_{e0} m_D v_{\phi 0} h_{nv}^{-1}}{\Gamma_\phi} = \frac{2\pi^2 \bar{a}^2 R^3 n_{e0} \bar{m} \Omega_{\phi 0}^{ex}}{\Gamma_\phi h_{nv}} \tag{2.15}$$

5

$$\Gamma_\phi = \frac{\sqrt{2\overline{m}_b}R_{tan}P_b}{\sqrt{E_b}}, \qquad (2.16)$$

where $h_{nv}^{-1} \equiv 1 + \alpha_n + \alpha_v$, Γ_ϕ is the torque input from NBI, R_{tan} is the tangency radius, E_b is the neutral beam energy, n_{e0} is the central electron density, $\Omega_{\phi 0}^{ex}$ is the central angular frequency, and $\overline{m}$ is an effective mass[11] which reduces to m_D for deuterium plasmas. The theoretical and experimental confinement times determined from Eqs. (2.12) and (2.15) can be compared in order to determine the validity of the asymmetry predictions.

2.2   Computational Model

As mentioned earlier, the set of six nonlinear equations was solved using a nonlinear equation solver. In this analysis, the equations were solved using HYBRID.[12] HYBRID is a general nonlinear equation solver which finds the zeros of a system of n nonlinear equations in n unknowns. The system of equations is provided by the user in the form of a subroutine to HYBRID. Solution of the equations is calculated by the forward-difference approximation. This section first describes the calculation of the input data, then the numerical computation of the asymmetries and confinement time.

2.2.1   Input Parameters

Prior to solving the system of equations, a few plasma parameters were calculated. First, for those cases in which the central electron density was not known, it was calculated from the line-average density $\bar{n}_e$ and the density profile factor α_n using numerical integration. Density, temperature, and velocity were then calculated at $r/a = 0.5$, where a is the minor radius. Radial profiles were assumed to be of the

form

$$x = x_0(1 - (r/a)^2)^{\alpha_x} \qquad (2.17)$$

where x=n, T, or v. However, in the case of DIII, the density[13] profile was given by

$$n_e = n_{e0}(1 - \frac{n_b}{n_{e0}})(1 - (r/a)^2)^{\alpha_n} + n_b. \qquad (2.18)$$

Next, the ratios of ion density (j=main ion, k=impurity ion) to electron density were calculated from the effective charge[9]

$$\frac{n_j}{n_e} = \frac{Z - Z_{eff}}{Z - 1} \qquad (2.19)$$

$$\frac{n_k}{n_e} = \frac{Z_{eff} - 1}{Z(Z - 1)} \qquad (2.20)$$

so that

$$\alpha = \frac{(n_k/n_e)Z^2}{(n_j/n_e)}. \qquad (2.21)$$

The dimensionless impurity ion species self-collision frequency[9] $\bar{\nu}_{kk}^*$ was

$$\bar{\nu}_{kk}^* = \nu_{kk}qR/v_{th,k} \qquad (2.22)$$

where the self-collision frequency[14] is defined as

$$\nu_{kk} = \frac{1.36 \times 10^{-7}n_j\alpha Z^2\Lambda}{\sqrt{m_k}T_k^{1.5}} \qquad (2.23)$$

$$Coulomb\ logarithm = \Lambda = 23 - \log\left[\frac{2Z^2\sqrt{2\alpha n_j}}{T_k^{1.5}}\right] \qquad (2.24)$$

and the impurity ion species thermal velocity[15] is

$$v_{thk} = 1.38 \times 10^6\sqrt{\frac{T_k}{m_k}}. \qquad (2.25)$$

Dimensionless toroidal velocities were calculated for each ion species[9]

$$\hat{v}_{\phi j} = \frac{\hat{v}_\phi^{ex}}{v_{thj}} \quad and \quad \hat{v}_{\phi k} = \frac{\hat{v}_\phi^{ex}}{v_{thk}}. \qquad (2.26)$$

7

using the ion thermal velocities of Eq. (2.25).

Finally, the above calculations were used to compute the dimensionless main ion self-collision frequency and the dimensionless interspecies collision frequencies[9]

$$\bar{\nu}_{jj}^{*} = \frac{\bar{\nu}_{kk}^{*}}{Z^2 \alpha} \tag{2.27}$$

$$\bar{\nu}_{jk}^{*} = \frac{\bar{\nu}_{kk}^{*}}{Z^2} \sqrt{\frac{m_j + m_k}{2m_k}} \tag{2.28}$$

$$\bar{\nu}_{kj}^{*} = \frac{\bar{\nu}_{kk}^{*}}{\alpha} \sqrt{\frac{m_j + m_k}{2m_j}} \tag{2.29}$$

2.2.2 Asymmetries and Theoretical Confinement Time

Appendix A includes a copy of the user subroutine, SUBROUTINE FCN, containing the system of six equations. The main computations were of the poloidal velocity and density asymmetries. Each of the six equations obtained from Eqs. (2.3-2.9) were rewritten with all terms on the left-hand-side of the equation such that the value of the right-hand-side was zero. The first execution of the subroutine resulted in an estimate of the roots of the system of nonlinear equations (using an initial guess of zero for each root). Subsequent calls to the subroutine yielded estimates of the roots until successive estimates varied by 10^{-5} or less for each root.

After solving the equations, SUBROUTINE FCN was called one final time. At this time, the predicted asymmetries were used to calculate the normalized poloidal and radial profile factors. Using these normalized profile factors, the theoretical momentum confinement time was calculated according to Eq. (2.12).

8

CHAPTER III

ANALYSIS OF EXPERIMENT

3.1 Experimental Parameters

The rotation velocities and density asymmetries of each tokamak were calculated by providing the nonlinear equation solver with values of the plasma parameters at r/a=0.5. Since the density, temperature, and velocity were calculated at a point halfway across the plasma minor radius, they were considered average values of the plasma characteristics, as were the other quantities determined from these parameters.

Most of the data available for each tokamak covered a range of values and a range of discharge types. The discharges selected for analysis had known experimental momentum confinement times and sufficient experimental data for the evaluation of the input parameters. However, information concerning some input parameters was unavailable and a few basic assumptions were made and applied to all tokamaks:

- Safety factor $q(r/a=0.5)=2$ since $q(0)\sim 1$ and $q(a)\sim 3$

- $\beta = B_\theta/B_\phi = 0.1$

- $e\Phi/T_i=1$

- Radial velocities $\hat{v}_{jr}$ and $\hat{v}_{kr}$ were zero

- Beam momentum inputs $\hat{M}_{\theta j}$ and $\hat{M}_{\theta k}$ were zero

- Radial profile has the form $x(r) = x_0(1 - (r/a)^2)^{\alpha_x}$

The value of $e\Phi/T_i = 1$ was obtained for ISX-B[16] at a potential of 0.5 V and an average ion temperature of 500 eV. Since measurements of electrostatic potential were not available for the other machines, the value of $e\Phi/T_i$ obtained for ISX-B was assumed to be a reasonable estimate for all machines.

Several other parameters which were different for each machine were necessary in solving for the density asymmetries and poloidal velocities. Some of the parameters were known, and others were calculated from the known quantities as discussed in Chapter II. Parameters such as plasma current and neutral beam power were not essential to the analysis of the data, but are included to illustrate the operating regime of each tokamak. The known parameters were central toroidal velocity, effective charge z_{eff}, ion-to-electron temperature ratio, profile factors α_x, major and minor radii, magnetic field, central ion temperature, and line-average density. In some cases the central electron density was known. The calculated parameters included ion and impurity densities, collision frequencies, thermal velocities, and in some cases, central electron density. Methods of determining these machine-dependent parameters are presented in the following subsections. The parameters that characterize the discharges analyzed in this thesis are given in Table 1. For perspective, the range of relevant experimental parameters achieved in these machines is given in Table 2.

3.1.1 Axially Symmetric Divertor Experiment

Two complete sets of data[17,18] were available for the analysis of deuterium discharges with a dominant carbon impurity in ASDEX. One set with $\Omega = 9.1 \times 10^4$ rad/s was suitable for analysis. The other with $\Omega = 2.3 \times 10^4$ rad/s did not satisfy the requirement that $v_\phi^{ex} \sim v_{th}$ and was not analyzed. Both data sets were part of a larger

set of data that covered a range of parametric values. In Table 2, z_{eff}, v_ϕ, T_{i0}, and P_b describe the two subsets of data; the remaining ranges of input parameters pertain to the larger data set.

By using the peaking factors Q_x, defined as the ratio of the central parameter x_0 to the volume-averaged parameter $< x >$, the profile factors α_x were easily obtained. The peaking factors for density, angular velocity, and electron temperature were given by[17]

$$Q_n = 1.6 \times (I_p/0.38)^{-0.35} \times (B_t/2.2)^{0.35} \qquad (3.1)$$

$$Q_\Omega = 2.3 \times (I_p/0.38)^{-0.45} \times (B_t/2.2)^{0.95} \qquad (3.2)$$

$$Q_{T_e} = 2.3 \times (I_p/0.38)^{-0.7} \times (B_t/2.2)^{0.7} \qquad (3.3)$$

where current has units of MA and magnetic field has units of T. Introducing a spatial integral[11] of the form

$$(h_x)^{-1} \equiv \frac{2}{a^2} \int_0^a [1 - (r/a)^2]^{\alpha_x} r dr \equiv \frac{2}{a^2} \int_0^a h_x(r) r dr = (1 + \alpha_x)^{-1} \qquad (3.4)$$

such that $x(r) = x_0 h_x(r)$, and defining an average quantity $< x >$

$$< x > \equiv \frac{\int_0^a x(r) r dr}{\int_0^a r dr} = x_0 (1 + \alpha_x)^{-1}, \qquad (3.5)$$

it is easily seen that the peaking factor Q_x is

$$Q_x \equiv \frac{x_0}{< x >} = 1 + \alpha_x. \qquad (3.6)$$

Due to the relatively high density in the case chosen for analysis, T_i and T_e were roughly equal.[18] Thus the ion temperature profile factor α_T was assumed to be approximated by the electron temperature profile factor calculated from Q_{T_e}.

3.1.2 Doublet III

The data for DIII were obtained for deuterium plasmas with a dominant oxygen impurity. Data covering a wide range of parameters were available; however, central

11

toroidal velocities were available only for specific sets of data.[13] Furthermore, plots of experimental momentum confinement times were only available for plasmas with characteristics different from the tabulated data.[19] Thus all of the tabulated data describing two different types of discharges was averaged and scaled, as described below, to obtain two cases for analysis.

The first case[13] was an average of the data from two similar shots at a current of about 0.7 MA and 3.9 MW NBI. The other case[13] was an average of the data from two similar shots at 0.71 MA and 6.1 MW NBI. Average parameters for both cases were calculated by averaging all of the data (including profile factors) for both pairs of shots. The ion temperatures were scaled using the relation

$$T = T_1 \frac{P_b \tau_\phi n_{e1}}{P_{b1} \tau_{\phi 1} n_e} \tag{3.7}$$

where the subscript 1 indicates values at $\bar{n}_e = 8 \times 10^{13}$ cm^{-3}. The scaling was necessary since the plots of experimental confinement times[19] were available only for $\bar{n}_e = 8 \times 10^{13}$ cm^{-3} whereas $\bar{n}_e$ for the tabulated data was lower. Straight-line fits to the plots of experimental confinement time versus beam power were not justifiable; τ_ϕ^{ex} varied slightly and inconsistently with P_b. Since τ_ϕ^{ex} varied little for small changes in P_b, the ratio of $P_b \tau_\phi$ to $P_{b1} \tau_{\phi 1}$ was set to unity in Eq. (3.7).

As mentioned earlier, the central velocities[19] were available for only specific sets of data, namely P_b=3.7, 5.0, and 5.9 MW, all at major radii of R=1.52, 1.67, and 1.74 m. The velocities at P_b=3.7 and 5.9 MW and a major radius of 1.52 m were chosen to describe the two cases at 3.9 and 6.1 MW (R~1.43 m).

Finally, profile factors α_x of the density, temperature, and velocity were determined from the central x_0 and midway $x_{r/a=0.5}$ values using the relation

$$\alpha_x = \frac{\ln\left[(x_{r/a=0.5})/(x_0)\right]}{\ln[1 - (r/a = 0.5)^2]}. \tag{3.8}$$

The temperature and velocity profiles were assumed to be parabolic to some power,

12

but the electron density was given by Eq. (2.18).

3.1.3 Impurity Studies Experiment-B

Analysis of ISX-B[16] began with determining the experimental toroidal velocity as a function of the neutral beam power. A straight-line fit to the data[16] yielded

$$v_\phi = (8.4995 + 2.365 P_b)(10^6) \tag{3.9}$$

with P_b in MW and v_ϕ in cm/s.

In ISX-B, the study focused on hydrogen neutral beam co-injection in deuterium plasmas with a dominant carbon impurity. The central ion temperature for such a plasma is given by[16]

$$T_i(0) = T_{OH}(0) + C\frac{P_b}{\bar{n}_e} \tag{3.10}$$

where $C = 2.2 \times 10^{-19}$ keV $\cdot$ MW$^{-1}\cdot$ m^{-3} for $H^\circ \rightarrow D^+$ NBI and $T_{OH}(0) = 0.3$ keV.

The experimental momentum confinement time was 17 ms at $P_b = 0.85$ MW and $\bar{n}_e = 4.5 \times 10^{13}$ cm^{-3}.[16] Using these parameters in Eqs. (3.9) and (3.10) yields $v_\phi^{ex} = 1.1 \times 10^7$ cm/s and $T_{i0} = 716$ eV.

3.1.4 Joint European Torus

Data for JET[11,20] covered both H-mode and L-mode deuterium plasmas with a dominant carbon impurity. For most H-mode discharges $\tau_\phi^{ex} = 200-500$ ms, and for most L-mode discharges $\tau_\phi^{ex} = 100-200$ ms.[11] However, ranges of experimental confinement times do not sufficiently indicate the accuracy of the theoretical model. For this reason, an experimental confinement time was constructed for one H-mode and one L-mode shot using the available data[20] and Eqs. (2.15) and (2.16). Using an average $R_{tan} = 1.515$ m (eight ion sources with $R_{tan} = 1.85$ m and eight with $R_{tan} = 1.18$ m),[11]

13

the experimental momentum confinement time was 204 ms for the H-mode shot and 70 ms for the L-mode shot.

Temperature profiles in L-mode discharges varied up to slightly more peaked than parabolic to the fourth power.[11] For this reason two values of α_T (3.5 and 4.0) were chosen to illustrate a range of predicted confinement times.

3.1.5 Princeton Large Torus

In PLT,[16] deuterium neutral beams were injected in a hydrogen plasma with a dominant carbon impurity. The analysis of PLT began similarly to that of ISX-B. The experimental toroidal velocity was plotted as a function of the neutral beam power over the square root of the beam energy. Since all of the PLT cases were for a beam energy of 40 keV, a curve was fit to v_ϕ versus $\sqrt{40P_b}$ with v_ϕ in cm/s and P_b in MW,[16] yielding

$$v_\phi = -2.143 \times 10^5 + 7.8683 \times 10^6 P_b. \tag{3.11}$$

The beam power[16] ranged up to 1.2 MW, thus the largest toroidal velocity in PLT did not satisfy $v_\phi^{ex} \sim v_{th}$ and no further analysis was performed. It should be noted, however, that the theory may be generalized to model cases in which v_ϕ^{ex} does not approach v_{th}.

3.1.6 Tokamak Fusion Test Reactor

Although several sets of TFTR data[21] were available for deuterium plasmas with a carbon impurity, only one included temperature, velocity, and density profiles. This case, a hot ion-mode discharge, was chosen for the analysis.

Determination of experimental momentum confinement time proceeded as for JET with Γ_ϕ=18.25 N·m in Eq. (2.16), yielding an experimental momentum confinement time of 44 ms. Profile factors were determined using the same method as for

14

DIII (Eq. (3.8)).

3.2 Momentum Confinement Results

Recent research has shown that the neoclassical (gyroviscous) theory[11] predicts momentum confinement times reasonably well. Until now, however, the application of this theory has involved the theoretical determination of the poloidal rotation and density asymmetries based on certain assumptions[11,21] about the normalized poloidal, $\tilde{\Theta}$, and radial, G, profile factors. Such assumptions were that the product $\tilde{\Theta}G=1$, or as in a recent study of TFTR, $\tilde{\Theta}=1.5$. In the present analysis, these profile factors were calculated from first principles using the predictions of the poloidal rotation velocity and density asymmetries of Eqs. (2.3-2.9) to evaluate Eqs. (2.13) and (2.14). As shown in Table 3 and Figure 1, the theoretical momentum confinement times closely predicted the experimental momentum confinement times. The term $(\tilde{\Theta}G/z)_{eff}$ in Eq. (2.12) ranged from 0.18 to 0.29 for Group 1 tokamaks and from 0.048 to 0.12 for Group 2 tokamaks. Thus $(\tilde{\Theta}G/z)_{eff} \sim O(0.1)$, with the main ions contributing slightly more than the impurity ion species to this parameter.

The division of the tokamaks into two distinct groups is illustrated in Figure 2 which shows the variation of the viscosity with the self-collision frequency ν^*. Two entries are shown for each experiment in Figure 2: the leftmost one for the plasma ions and the rightmost one for the impurity ions. The value of the impurity ion self-collision frequency $(\tilde{\nu}_{kk}^*)$ is greater than the value of the main ion self-collision frequency $(\tilde{\nu}_{jj}^*)$ for both groups, thus the main ions are less collisional than the impurity ions and $f_{jGroup2} < f_{jGroup1} < f_{kGroup2} < f_{kGroup1}$. We also note that since the predictions of τ_ϕ are based entirely on neoclassical theory, the results shown in Table 3 and Figure 1 demonstrate agreement between a first-principles calculation of τ_ϕ and experiment.

The close agreement of the confinement times provides some measure of con-

Table 1: Summary of Machine Parameters and Plasma Characteristics.

Machine	Ref.	Parameters												
		R (m)	a (m)	I_p (MA)	P_b (MW)	B_ϕ (T)	$v_\phi^{ex}(0)$ ($10^7 \frac{cm}{s}$)	$T_i(0)$ (keV)	$\frac{T_i}{T_e}$	$\bar{n}_e$ ($\frac{10^{13}}{cm^3}$)	z_{eff}	α_n	α_v	α_T
ASDEX	[17,18]	1.65	0.40	0.42	1.8	2.17	1.5	1.23	1.0	4.6	3.2	0.54	1.2	1.1
DIII	[13,19]	1.43	0.385	0.7	3.85	2.53	1.2	1.89	1.0	8.0	1.85	0.97	0.99	2.0
	[13,19]	1.44	0.38	0.71	6.1	2.53	1.6	2.23	0.97	8.0	2.0	0.96	1.1	1.9
ISX-B	[16]	0.93	0.25	0.155	0.85	1.4	1.1	7.16	1.0	4.5	2.5	1.0	1.0	1.0
JET (H)	[11,20]	3.00	1.10	3.1	7.7	2.2	2.0	5.5	1.25	3.0	2.3	0.0	1.5	1.5
JET (L)	[11,20]	3.00	1.10	3.22	14.25	3.47	3.5	15.5	1.5	1.33	3.5	2.0	3.0	3.5–4.0
TFTR	[21]	2.45	0.79	1.1	11.6	4.75	6.2	26.0	2.2	2.0	3.1	1.0	3.9	4.3

Table 2: Ranges of Experimental Parameters.

Machine	Ref.	Parameters						
		I_p (MA)	P_b (MW)	B_ϕ (T)	$v_\phi^{ex}(0)$ (10^7cm/s)	$T_i(0)$ (keV)	$\bar{n}_e$ (10^{13}cm^{-3})	z_{eff}
ASDEX	[17,18]	0.25–0.45	0.3–1.8	1.87–2.8	2.3–9.1†	1.05–1.23	1.6–7.6	2.6–3.2
DIII	[13,19]	0.35–0.89	3.7–6.1	2.53	1.2–1.6	1.72–3.79	3.3–8.0	1.8–3.2
ISX-B	[16]	0.155	0.2–2.0	1.4	0.9–1.3	0.4–1.3	4.5	2.5
JET	[11,20]	>3	4–15	2.2–3.5	2–13‡	3.5–17.5	2.5–8.2†	2–4
TFTR	[21]	1.1–1.8	4.4–13.6	4.75	2.4–5.5	9.6–21.7	1.4–2.8	3–4

† $\Omega(\times 10^4$rad/s)   ‡ n_{e0}

Table 3: Comparison of Momentum Confinement Times.

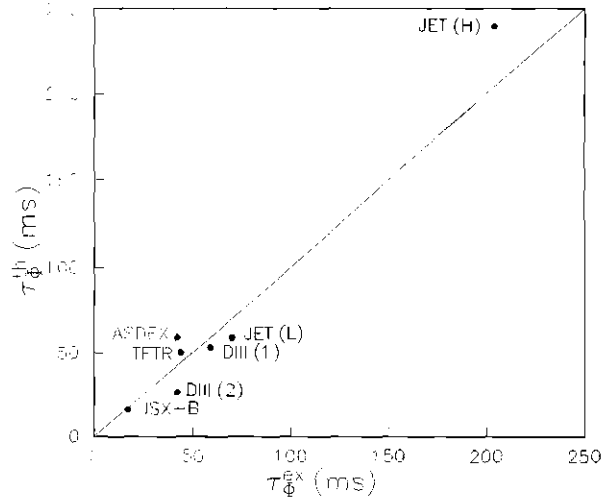| Machine	I_p (MA)	P_b (MW)	B_ϕ (T)	$v_\phi^{ex}(0)$ $(10^7 \frac{cm}{s})$	$T_i(0)$ (keV)	$\bar{n}_e$ $(\frac{10^{13}}{cm^3})$	τ_ϕ^{ex} ms	τ_ϕ^{th} ms
ASDEX	0.42	1.8	2.17	1.5	1.23	4.6	42	59
DIII	0.7	3.85	2.53	1.2	1.89	8.0	59	53
DIII	0.71	6.1	2.53	1.6	2.23	8.0	42	26
ISX-B	0.155	0.85	1.4	1.1	7.16	4.5	17	16
JET (H-mode)	3.1	7.7	2.2	2.0	5.5	3.0	204	240
JET (L-mode)	3.22	14.25	3.47	3.5	15.5	1.33	70	58–89
TFTR	1.1	11.6	4.75	6.2	26.0	2.0	44	50

Figure 1: Comparison of Theoretical and Experimental Momentum Confinement Times.
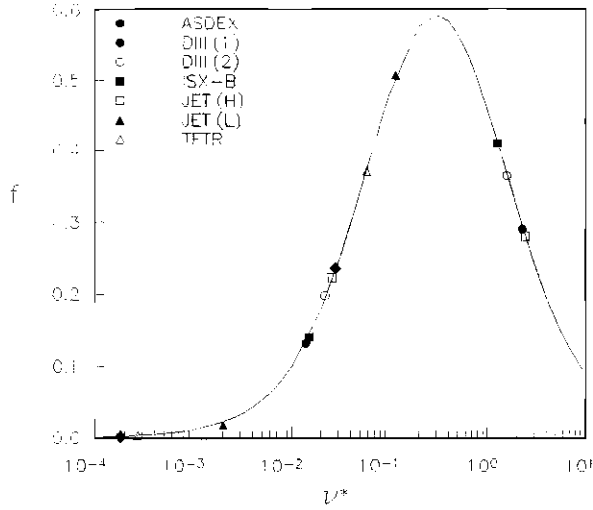
Figure 2: Viscosity as a Function of Self-collision Frequency.

fidence that the predicted asymmetries reasonably approximate the actual plasma asymmetries. The results of the poloidal rotation and density asymmetry analysis are therefore presented in the following sections.

3.3 Poloidal Rotation and Density Asymmetry Results

Before proceeding with the analysis of the asymmetries, it is interesting to note that T_{i0}, $v_{\phi 0}$, P_b, and I_p were higher for discharges in the large machines (TFTR and JET), while n_{e0} was higher in the smaller machines (ASDEX, DIII, and ISX-B). This grouping of machines—ASDEX/DIII/ISX-B (Group 1) and TFTR/JET (Group 2)— occurs frequently throughout the tables and figures. The values of the asymmetries are shown in Table 4 and their dominant driving forces are summarized in Table 5.

18

Table 4: Poloidal Rotation and Density Asymmetries.

Machine	$\hat{v}_{j\theta}$	$\hat{v}_{k\theta}$	$\tilde{n}_j^c/\epsilon$	$\tilde{n}_k^c/\epsilon$	$\tilde{n}_j^s/\epsilon$	$\tilde{n}_k^s/\epsilon$
ASDEX	-0.15	-0.35	0.064	0.38	0.0087	0.061
DIII (1)	-0.063	-0.17	0.057	0.45	0.011	0.040
DIII (2)	-0.11	-0.27	0.073	0.57	0.0073	0.12
ISX-B	-0.13	-0.32	0.075	0.46	0.030	0.037
JET (H)	-0.047	-0.073	0.035	0.21	-0.0049	0.045
JET (L)	-0.11	-0.075	0.028	0.17	-0.0056	0.024
TFTR	-0.12	-0.079	0.047	0.28	-0.0031	0.023

Table 5: Summary of Asymmetries and Driving Forces.

Asymmetry	Group 1	Group 2
$\hat{v}_{j\theta}$	$\bar{\nu}_{jj}^*$	$\bar{\nu}_{jj}^*, \hat{v}_{j\phi}^{ex}$
$\hat{v}_{k\theta}$	$\bar{\nu}_{kk}^*, \bar{\nu}_{kj}^*, \hat{v}_{k\phi}^{ex}$	$\bar{\nu}_{kk}^*$
$\tilde{n}_j^s$	$\bar{\nu}_{jj}^*$	$\tilde{\Phi}^s$
$\tilde{n}_k^s$	$\bar{\nu}_{kk}^*$	$\bar{\nu}_{kk}^*, \hat{v}_{k\phi}^{ex}$
$\tilde{n}_j^c$	$\hat{v}_{j\phi}^{ex}$	$\hat{v}_{j\phi}^{ex}$
$\tilde{n}_k^c$	$\hat{v}_{k\phi}^{ex}$	$\hat{v}_{k\phi}^{ex}$

3.3.1 In-out and Up-down Density Asymmetries

The density asymmetries, defined[9] as

$$\tilde{n}(r) \equiv [n(r,\theta) - \bar{n}(r)]/[\bar{n}(r)], \tag{3.12}$$

are less than the inverse aspect ratio ϵ in all cases. While $\tilde{n}_k^c$ ranges from 0.17ϵ to 0.57ϵ, $\tilde{n}_j^c$ and $\tilde{n}_k^s$ are much smaller and range from 0.023ϵ to 0.12ϵ. The smallest density asymmetry relative to ϵ is $\tilde{n}_j^s$, the magnitude of which is in the range 0.0031ϵ–0.03ϵ.

The analysis begins with the effect of the plasmas's inertia due to the toroidal velocity, or the centrifugal force. As the main ion and impurity ion species rotate in the toroidal direction (i.e., along the minor axis), inertial effects are expected to increase the density of the ions on the outboard side of the tokamak. This outward shift corresponds to $\tilde{n}^c > 0$. Evaluation of each term coupling the density asymmetries showed that the largest term contributing to both $\tilde{n}_j^c$ and $\tilde{n}_k^c$ was indeed the inertia $\hat{v}_{j\phi}^{ex}$, with j representing either the main ion or impurity ion. Furthermore, the in-out density asymmetries are positive and increase with increasing values of the toroidal velocity, as would be expected. The inertial term also contributed to the up-down impurity density asymmetry for Group 1, again with $\tilde{n}_k^s$ increasing with increasing v_ϕ.

The viscosity (f_j, f_k), which is a function of the self-collision frequency ($\bar{\nu}_{jj}^*$, $\bar{\nu}_{kk}^*$), contributed to the impurity ion $\tilde{n}^s$ for both Groups. Although $\tilde{n}_k^s$ remained constant for increasing f, $\tilde{n}_j^s$ increased for Group 1. The largest contributor to Group 2 $\tilde{n}_j^s$ was the potential asymmetry $\tilde{\Phi}^s$.

An increase in the ion density near the top of a tokamak corresponds to $\tilde{n}^s > 0$. Thus the up-down density asymmetries for the Group 1 main ion species and all of the impurity ion species show an upward shift. However, the up-down density asymmetries for the main ion species are negative for Group 2 tokamaks, indicating a downward shift of ions.

20

As a whole, the magnitudes of the in-out and the up-down asymmetries for both species were smallest for Group 2 tokamaks.

3.3.2 Poloidal Velocity

Analysis of Eq. (2.3) showed that the viscosity terms contributed to the poloidal velocity in all cases. The dependence of the poloidal velocities on the viscosity was non-monotonic; a result easily explained by the additional dependence of $\hat{v}_{k\theta}$ on ν^* and $\hat{v}_\phi$ for Group 1 and of $\hat{v}_{j\theta}$ on $\hat{v}_\phi$ for Group 2. In general, the poloidal velocities were smallest for Group 2. Furthermore, all values of v_θ were less than zero, indicating rotation opposite to the direction of B_θ for both species.

CHAPTER IV

DISCUSSION OF RELATED THEORIES

In the case of a non-rotating plasma with the main ion and the high z impurity ion in the collisional regime, Chang and Hazeltine[22] used the momentum balance equation (neglecting inertia, source, and viscous terms) to show that the density and potential asymmetries were related to the friction term $\bar{\nu}_{jk}^*$. However, the numerical analysis in Chapter III showed that the density asymmetries depended mainly on the ion self-collision frequencies.

Neglecting the viscous and source term in the momentum balance equation, Burrell et al.[23] derived expressions for the density asymmetries with the following assumptions:

- large aspect ratio

- $m_k/m_j \ll 1$ $\left(v_{thk} \sim v_\phi \ll v_{thj}\right)$

- $n_k z^2/n_j \ll 1$

With the above assumptions,

$$\tilde{n}_k^s \sim \frac{m_j q^2 R z^2 \bar{\nu}_{jj}^*}{eB_\phi L_n} = \epsilon \frac{qR\bar{\nu}_{jj}^* z^2}{v_{thj}}\delta_{\theta j} \quad and \quad \tilde{n}_k^c \sim \epsilon \frac{m_k v_\phi^2}{T_k}. \tag{4.1}$$

Therefore $\tilde{n}_k^s$ and $\tilde{n}_k^c$ were driven by viscosity $f_j(\bar{\nu}_{jj}^*)$ and inertia, respectively, as was shown in Chapter III.

Hsu and Sigmar[24] derived density asymmetries in a strongly rotating plasma with two ion species in the Pfirsch-Schlüter regime. They found that

$$\tilde{n}_j^c \sim \epsilon v_{\hat{\Phi}_j}^2 / v_{thj}^2 \quad and \quad \tilde{n}_k^s = \frac{2\epsilon\mu z^2}{1 + \mu^2 z^4} \tag{4.2}$$

where $\mu = \mu(T_e, T_i, D, p)$. Thus inertia drives $\tilde{n}_j^c$ and parallel friction $(\bar{\nu}_{jk}^*)$ drives $\tilde{n}_k^s$. While $\tilde{n}_j^c$ was found to depend on inertia in Chapter III, the ion self-collision frequency, not the interspecies collision-frequency, contributed to $\tilde{n}_k^s$.

CHAPTER V

CONCLUSIONS AND RECOMMENDATIONS

Based on the agreement between predicted and experimental momentum confinement times, the theory appears to adequately describe the poloidal rotation and density asymmetries of the main ion and impurity ion species present in tokamak plasmas. Thus the physical mechanisms identified as the dominant driving forces of plasma asymmetries must also be reasonably correct.

The dominant mechanism contributing to the in-out density asymmetries was the inertia, while the viscosity was the main driving force in the up-down asymmetries, with additional contributions arising from potential asymmetries. Viscosity, inertia, and friction all contributed in varying degrees to the poloidal rotation velocities. In general, the dependence of the asymmetries on individual forces was not readily identifiable, except for the in-out density asymmetries which increased with increasing toroidal velocity.

The poloidal velocities were $O(10^{-1})$, except for the Group 2 impurity ion species velocities which were $O(10^{-2})$. The in-out density asymmetries for the main ion species and the up-down density asymmetries for the impurity ion species were also $O(10^{-2})$. The impurity ion in-out density asymmetries were larger than those for the main ion species and were about $O(10^{-1})$. The up-down density asymmetries of the main ion species were about $O(10^{-3})$.

Future investigations of the poloidal asymmetry theory would be enhanced by the increasing availability of complete plasma databases. As radial measurements of density, temperature, and velocity improve, the parabolic profile assumption should be replaced with actual fits to the data. Safety factor profiles should also be considered in future analyses. In addition, the electrostatic potential of a given tokamak should be measured and used in evaluating $e\Phi/T$ for that machine.

In conclusion, the theory predicts the asymmetries reasonably well, based on the results of the confinement analysis. However, comparison of the predicted asymmetries with actual measurements will give the best indication of the validity of the theory.

ACKNOWLEDGEMENTS

APPENDIX A

SUBROUTINE FCN

```
subroutine fcn (n,x,fvec,iflag,istar,vthetaj,vthetak)

integer n,iflag,istar,style

double precision x(n),fvec(n),q,beta,rnukj,alpha,zj,rmk,
*   rmj,rmjtheta,rmktheta,vjrad,vkrad,vphiex0,q2,vphiexk2,
*   beta2,vphiexj2,ep,fj,fk,rnujk,phij,phik,c1,c2,c3,c4,c5,
*   c6,phic,phis,thetaz,thetai,alphan,alphav,zk,
*   vthetaj,vthetak,rnujj,rnukk,alphat,zeff,G,thetagz,rne0,
*   ephiti,rmajor,rminor,temp0,bphi,hntv,hnv,rmd,rmdbar,rne,
*   tauphi,rovera2,vphiexj,vphiexk,titote,rnebar,densrat,
*   rnztone,rnitone

character tok*40, inform*60

c   read in data on initial run
    if(istar.eq.1)then
       open(unit=1,file='xsecin')
       istar=2
       read(1,'(a40)')tok
       read(1,'(a60)')inform
       read(1,'(i3)')style
       read (1,*) rnukk, vjrad, vkrad, vphiex0, vphiexj, vphiexk
       write(2,'(" nuzzstar     vzrad        virad     vphiex0")')
       write(2,'(d10.3,3x,f6.3,6x,f6.3,6x,d10.3)')
*      rnukk,vjrad,vkrad,vphiex0
       if(style.eq.3)then
           read (1,*) alpha, q, zeff, titote, densrat
       else
           read (1,*) alpha, q, zeff, titote
       endif
       write(2,*)
```

```fortran
      write(2,'("alpha          q            zeff       Ti/Te")')
      write (2,5) alpha, q, zeff,titote
      read (1,*) zk, rmk, zj, rmj, beta
      write(2,*)
      write(2,'("zimp          massz        zion     massion")')
      write (2,5) zk, rmk, zj, rmj
      read (1,*) ephiti, rmjtheta, rmktheta, rnztone, rnitone
      write(2,*)
      write(2,'("e*phi/Ti       Mitheta     Mztheta")')
      write (2,5) ephiti, rmjtheta, rmktheta
5     format (4(f6.3,7x))
      read (1,*) alphan, alphav, alphat, rne0
      write(2,*)
      write(2,'("alphan         alphav       alphat      ne0")')
      write (2,15) alphan, alphav, alphat, rne0
15    format(3(f6.3,7x),d10.3)
      read (1,*) rovera2, rmajor, bphi, temp0, rnebar
      write(2,*)
      write(2,'("(r/a)^2      major radius     bphi        Tion(0)
     *nebar")')
      write (2,12) rovera2, rmajor, bphi, temp0, rnebar
12    format (f6.3,7x,f6.3,8x,f6.3,4x,f10.3,4x,d10.3)
      read (1,*) rmd, rmdbar, rne, rminor
      write(2,*)
      write(2,'("m sub D      m sub d bar    minor radius  ")')
      write (2,9) rmd, rmdbar, rminor
9     format (f6.3,8x,f6.3,7x,f6.3)
      read(1,*) rnujj, ep, fk, fj, rnujk, rnukj
      read(1,*) phij, phik
      read(1,*) c1, c2, c3, c4, c5, c6
      write(2,*)
      write(2,'("nuii star=",d10.3)')rnujj
      write(2,'("epsilon=",d10.3)')ep
      write(2,'("f ion and f impurity: ",2(d10.3))') fj, fk
      write(2,'("ion-impurity and impurity-ion collision freq: ",
     *    d10.3,3x,d10.3)')rnujk, rnukj
      write(2,'("phii hat and phiz hat:",d10.3,3x,d10.3)')
     *    phij,phik
      close(1)
      beta2=beta*beta
      q2=q*q
      vphiexj2=vphiexj*vphiexj
      vphiexk2=vphiexk*vphiexk
```

```fortran
      endif
c  begin calculation of roots
      if(istar.eq.1 .or. istar.eq.2)then
c  potential asymmetries
      phic=(x(5)/c2+x(6)/c1)/(ephiti*titote)
      phis=(x(3)/c2+x(4)/c1)/(ephiti*titote)
c  user-supplied system of equations
      fvec(1)=x(1)*(q2*fj*(1.0d0 + 5.0d0*x(5)/6.0d0
     *          + 2.0d0*x(3)/3.0d0 + 1.0d0*x(3)*x(3)/3.0d0
     *          + 1.0d0*x(5)*x(5)/3.0d0 + phis*x(3)/2.0d0
     *          + 0.5d0*phic*(5.0d0+x(5))) + rnujk
     *          - q2*vphiexj*(x(3)+phis))
     *          - rmjtheta - vjrad - c5*x(2) + q2*vphiexj2
     *          * phis + 0.5d0*q2*fj*vphiexj*(phis*x(3)
     *          + phic*(5.0d0 + x(5)))

      fvec(2)=x(2)*(q2*fk*(1.0d0 + 5.0d0*x(6)/6.0d0
     *          + 2.0d0*x(4)/3.0d0 + 1.0d0*x(4)*x(4)/3.0d0
     *          + 1.0d0*x(6)*x(6)/3.0d0 + phis*x(4)/2.0d0
     *          + 0.5d0*phic*(5.0d0+x(6))) + rnukj
     *          - q2*vphiexk*(x(4)+phis))
     *          - rmktheta - vkrad - c6*x(1) + q2*vphiexk2
     *          * phis + 0.5d0*q2*fk*vphiexk*(phis*x(4)
     *          + phic*(5.0d0 + x(6)))

      fvec(3)=c3*x(1)*x(3) + vphiexj2 - 0.5d0*x(5)
     *          - 0.5d0*phij*phic + beta2*rnujk*x(1)*x(4)

      fvec(4)=c4*x(2)*x(4) + vphiexk2 - 0.5d0*x(6)
     *          - 0.5d0*phik*phic + beta2*rnukj*x(2)*x(3)

      fvec(5)=x(1)*c3*x(5) + x(1)*fj + 0.5d0*x(3) + 0.5d0*phij*phis
     *          - beta2*rnujk*x(1) + beta2*c5*x(2)
     *          + beta2*rnujk*x(1)*x(6) + beta2*vjrad

      fvec(6)=x(2)*c4*x(6) + x(2)*fk + 0.5d0*x(4) + 0.5d0*phik*phis
     *          - beta2*rnukj*x(2) + beta2*c6*x(1)
     *          + beta2*rnukj*x(2)*x(5) + beta2*vkrad
      endif
c  after solving equations, calculate confinement time
      if(istar.eq.3)then
        phic=(x(5)/c2+x(6)/c1)/(ephiti*titote)
        phis=(x(3)/c2+x(4)/c1)/(ephiti*titote)
```

```
            write(2,'("phic and phis: ",d10.3,3x,d10.3)') phic, phis
c   poloidal profile factors
            thetaz=(4.0d0+x(6))*((-x(2)*(phis+x(4))/vphiexk)
     *          + phis) + x(4)*((x(2)*(2.0d0+phic
     *          + x(6))/vphiexk) - phic)
            thetai=(4.0d0+x(5))*((-x(1)*(phis+x(3))/vphiexj)
     *          + phis) + x(3)*((x(1)*(2.0d0+phic
     *          + x(5))/vphiexj) - phic)
            write(2,'("theta z and theta ion: ",d10.3,3x,d10.3)')
     *      thetaz, thetai
c   radial profile factor for DIII
            if(style.eq.3)then
                G=2.0d0*rovera2*(alphan+alphav+alphat)*(1.0d0+densrat*
     *          ((alphat+alphav)*((1.0d0-rovera2)**(-alphan)))/
     *          (alphan+alphat+alphav) - 1.0d0))/
     *          ((1.0d0-rovera2)*(1.0d0 + densrat*(((1.0d0-rovera2)**
     *          (-alphan)) - 1.0d0)))
c   radial profile factor for other tokamaks
            else
                G=2.0d0*rovera2*(alphan+alphav+alphat)/
     *          (1.0d0-rovera2)
            endif
            write(2,'("G: ",d10.3)') G
            thetagz=(rnztone*thetaz + rnitone*thetai)*G
            write(2,10)thetagz
10          format('(theta*G/z)eff = ',d10.3)
            hntv=1.0d0+alphan+alphat+alphav
            hnv=1.0d0+alphan+alphav
            rmajor2=rmajor*rmajor
c   theoretical momentum confinement time (msec):
c   major radius (rmajor) in meters, toroidal magnetic field
c   (bphi) in Tesla, central ion temperature (temp0) in electron
volts
c       DIII
            if(style.eq.3)then
                tauphi=2.0d3*rmajor2*bphi*(1.0d0+alphat/(1.0d0+
     *          alphan+alphav))*(1.0d0+densrat*alphan/(1.0d0+
     *          alphav))*rmdbar/
     *          (temp0*(1.0d0 +densrat*alphan/(1.0d0+alphav+
     *          alphat))*rmd*thetagz)
c     other tokamaks
            else
                tauphi=2.0d3*rmajor2*bphi*hntv*rmdbar/
```

```
     *                    (temp0*hnv*rmd*thetagz)
         endif
         write(6,'(a40, "tauphi = ",f7.0)')tok,tauphi
         write(2,20)tauphi
20     format('theoretical momentum confinement time (msec)  =',
     f9.2)
         write(2,*)
         write(2,*)
     endif

     return
     end
```

BIBLIOGRAPHY

[1] R. J. Groebner, K. H. Burrell, and R. P. Seraydarian, *Physical Review Letters*, **64**, 3015 (1990).

[2] F. Wagner, F. Ryter, and A. R. Field et al., *Proceedings of the 13th International Conference Plasma Physics and Controlled Fusion Research*, Washington, IAEA (1991).

[3] Y. Miura, H. Aikawa, and K. Hoshino et al., *Proceedings of the 13th International Conference Plasma Physics and Controlled Fusion Research*, Washington, IAEA (1991).

[4] S. L. Allen, H. W. Moos, R. K. Richards, J. L. Terry, and E. S. Marmar, "The influence of the limiter on EUV emissions from light impurities in the Alcator A tokamak," *Nuclear Fusion*, **21**, 251–255 (1981).

[5] S. Suckewer et al., "Rapid scanning of spatial distribution of spectral line intensities in PLT tokamak," Technical Report PPPL-1430, Princeton Plasma Physics Laboratory (1978).

[6] K. Brau, S. Suckewer, and S. K. Wong, "Vertical poloidal asymmetries of low-Z element radiation in the PDX tokamak," *Nuclear Fusion*, **23**, 1657–1668 (1983).

[7] P. Smeulders, "Tomography of quasi-static deformations of constant-emission surfaces of high-beta plasmas in ASDEX," *Nuclear Fusion*, **26**, 267–273 (1986).

[8] K. W. Wenzel, *Bulletin of the American Physical Society*, **34**, 2153 (1989).

[9] W. M. Stacey, "Poloidal rotation and density asymmetries in a tokamak plasma with strong toroidal rotation," Technical Report GTFR 101, Georgia Institute of Technology (January 1992), *The Physics of Fluids B*, to be published.

[10] S. P. Hirshman and D. J. Sigmar, "Neoclassical transport of impurities in tokamak plasmas," *Nuclear Fusion*, **21**, 1079–1201 (1981).

[11] W. M. Stacey, "Interpretation of measurements of the global momentum and energy confinement times in strongly rotating tokamak plasmas," *Nuclear Fusion*, **31**, 31–49 (1991).

[12] B. S. Garbow, K. E. Hillstrom, and J. J. Moré, HYBRID, Minpack Project, ANL-80-74, Argonne National Laboratory (March 1980).

[13] A. J. Groebner, W. Pfeiffer, F. P. Blau, K. H. Burrell, E. S. Fairbanks, R. P. Seraydarian, H. St. John, and R. E. Stockdale, "Experimentally inferred ion thermal diffusivity profiles in the Doublet III tokamak," *Nuclear Fusion*, **26**, 543–554 (1986).

[14] D. L. Book, NRL Plasma Formulary (1990).

[15] W. M. Stacey, *Fusion Plasma Analysis*, John-Wiley and Sons (1981).

[16] W. M. Stacey, C. M. Ryu, and M. A. Malik, "Analysis of the unbalanced NBI rotation experiments in the ISX-B, PLT and PDX tokamaks," *Nuclear Fusion*, **26**, 293–302 (1986).

[17] A. Kallenbach, H. M. Mayer, G. Fussmann, V. Mertens, U. Stroth, and O. Vollmer and the ASDEX Team, "Characterisation of the angular momentum transport in ASDEX," Technical Report IPP I/255, Max-Planck-Institut für Plasmaphysik (October 1990).

[18] A. Kallenbach, Personal communication (July 1992).

[19] K. H. Burrell, R. J. Groebner, H. St. John, and R. P. Seraydarian, "Confinement of angular momentum in divertor and limiter discharges in the Doublet III tokamak," *Nuclear Fusion*, **28**, 3–15 (1988).

[20] W. M. Stacey, "Convective and viscous fluxes in strongly rotating tokamak plasmas," *Nuclear Fusion*, **30**, 2453–2465 (1990).

[21] G. Pautasso, *Analysis of a dedicated rotation experiment in TFTR*, PhD thesis, Georgia Institute of Technology, January 1992.

[22] C. S. Chang and R. D. Hazeltine, "Impurity transport in the collisional regime for large poloidal variations," *Nuclear Fusion*, **20**, 1397–1405 (1980).

[23] K. H. Burrell et al., *Physical Review Letters*, **47**, 511 (1981).

[24] C. T. Hsu and D. Sigmar, "Momentum transport in rotating tokamak plasmas including strong impurity ordering," *Bulletin of the American Physical Society*, **33**, 1938 (1988).